Soliton approximation in continuum models of leader-follower behavior

F. Terragni [1,2] W. D. Martinson [3] M. Carretero [1,2] P. K. Maini [3] and L. L. Bonilla [1,2,*]

[1] *Gregorio Millán Institute for Fluid Dynamics, Nanoscience and Industrial Mathematics, Universidad Carlos III de Madrid, 28911 Leganés, Spain*

[2] *Department of Mathematics, Universidad Carlos III de Madrid, 28911 Leganés, Spain*

[3] *Wolfson Centre for Mathematical Biology, Mathematical Institute, University of Oxford, Oxford OX2 6GG, United Kingdom*

(Received 28 July 2023; accepted 17 October 2023; published 14 November 2023)

Complex biological processes involve collective behavior of entities (bacteria, cells, animals) over many length and time scales and can be described by discrete models that track individuals or by continuum models involving densities and fields. We consider hybrid stochastic agent-based models of branching morphogenesis and angiogenesis (new blood vessel creation from preexisting vasculature), which treat cells as individuals that are guided by underlying continuous chemical and/or mechanical fields. In these descriptions, leader (tip) cells emerge from existing branches and follower (stalk) cells build the new sprout in their wake. Vessel branching and fusion (anastomosis) occur as a result of tip and stalk cell dynamics. Coarse graining these hybrid models in appropriate limits produces continuum partial differential equations (PDEs) for endothelial cell densities that are more analytically tractable. While these models differ in nonlinearity, they produce similar equations at leading order when chemotaxis is dominant. We analyze this leading order system in a simple quasi-one-dimensional geometry and show that the numerical solution of the leading order PDE is well described by a soliton wave that evolves from vessel to source. This wave is an attractor for intermediate times until it arrives at the hypoxic region releasing the growth factor. The mathematical techniques used here thus identify common features of discrete and continuum approaches and provide insight into general biological mechanisms governing their collective dynamics.

DOI: 10.1103/PhysRevE.108.054407

I. INTRODUCTION

The interplay between discrete and continuum approaches informs our understanding of many biological processes, such as morphogenesis [1–8], aggregation and swarming [9–14], pattern formation [15,16], bacterial motion [17,18], tissue repair [19–21], tumor invasion, and metastasis [2,22–24]. These phenomena all display elements of collective behavior, in which groups adopt unique behaviors not observed in smaller numbers of individuals. This comprises a central area of interest for soft and active matter physics, but collective cell behavior has the additional complexity that cell groups have the ability to adopt a wide variety of fluidlike, solidlike, or even glasslike states by undergoing so-called flocking and jamming transitions [25–29]. Consequently, the mechanisms underlying collective phenomena remain poorly understood in general. Some insight may be provided by mathematical modeling, as it provides an abstract setting in which to evaluate different hypotheses. Two approaches are largely used to represent cells in a collective. One approach, known as discrete modeling, involves tracking the evolution of each individual cell [30,31]. Due to the ability of these discrete approaches to represent each member of a collective, many biological mechanisms can be straightforwardly incorporated into discrete approaches and be directly tested in the laboratory. However, the long-time behavior of these models is usually difficult to ascertain without extensive and costly computation. This motivates the second type of modeling approach, which involves representing the whole population as a continuous function that evolves in space and time according to a set of partial differential equations (PDEs). While continuum approaches typically describe the ensemble average behavior of a collective, and hence cannot be used in general to resolve individual cells, these models are much faster to simulate, more amenable to analysis, and can provide insight into the important mechanisms governing the phenomenon of interest. For processes spanning many length and time scales, a combination of discrete and continuum approaches can be particularly useful.

An important example of a biological phenomenon in which mathematical modeling has helped uncover important underlying mechanisms is angiogenesis, the process by which new blood vessels grow from existing vasculature. This complex multiscale process is the basis of organ growth and regeneration, tissue repair, and wound healing in healthy conditions [32–38]. Disruptions to the natural balance of pro and antiangiogenic factors, by contrast, are linked with various pathological diseases such as cancer, diabetes, and retinopathies [37,39–43]. Angiogenesis is triggered by hypoxic (oxygen-lacking) cells that secrete diffusible growth factors which travel to nearby primary blood vessels. The binding of these growth factors to endothelial cells lining the primary vessel causes the latter to detach, move toward the hypoxic region, and build capillaries which transport blood, oxygen and nutrients. A growing capillary is led by

*Corresponding author: bonilla@ing.uc3m.es

so-called "tip" cells that sense and move up the gradient of growth factors, in a process known as chemotaxis, to reach the hypoxic region. Stalk cells proliferate along the path of tip cells and construct the nascent capillary. A tip cell may encounter another tip cell or growing capillary during the course of migration; when it does so, it fuses with the object in a process called "anastomosis" which results in the new vessel forming a closed loop that supports blood flow. Tip cells may also emerge along the length of capillaries, which enables the creation of multiple branches in the new network.

Mathematical models of angiogenesis capture these dynamics of cell movement, branching, and anastomosis by describing tip and stalk cells as leaders and followers, respectively. In addition to angiogenesis, such leader-follower frameworks are important in explaining aspects of morphogenesis [3,4,6,7] and wound healing [44–46]. Multiple types of frameworks have been constructed to describe angiogenesis, ranging from continuum approaches described by PDEs [47–52] to discrete approaches using agent-based models (ABMs) [43,53–63], mesoscale approaches relying on tools from kinetic theory [64], or hybrid approaches combining aspects of discrete and continuum frameworks to simulate cells and their microenvironment [65–67]. One important discrete model for angiogenesis, for instance, examined minimal mechanisms that could lead to the branched vessel networks resembling those observed in vivo [52]. Continuum models of angiogenesis have also quantified how chemotaxis and branching determined the speed and distribution of tip cells [50]. For further information about mathematical modeling of angiogenesis, we refer to the following reviews [52,68–78].

One drawback of many continuum models used to simulate angiogenesis is that the equations are constructed with a phenomenological "top-down" approach, which involves deducing the PDEs through principles such as the conservation of mass, energy, etc. For example, so-called "snail-trail" models consider nonlinear stalk cell proliferation along tip cell trajectories [48,50,73,79,80] and are inspired by mathematical frameworks used to study branching patterns in fungal growth [81]. Consequently, these continuum models can be difficult to link to the underlying biology and can be deceptively difficult to analyze, even though they form a mathematically interesting paradigm for leader-follower behavior. This motivated the derivation of "coarse-grained" PDEs, which can be obtained by investigating the ensemble average behavior of cell-based angiogenesis models using techniques from statistical mechanics [74,82–95]. While different ABMs can lead to quite different continuum equations [89,92], methods from asymptotic analysis [95] show that there are parameter regimes for which these different continuum models produce identical dynamics at leading order. These "leading order" PDEs (LO-PDEs) suggest a shared set of mechanisms that are inherent to the leader-follower dynamics exhibited in angiogenesis and admit traveling wave solutions of time-varying amplitude, which in certain cases may be approximated by self-similar solutions.

Our main result in this paper is that the LO-PDEs in simple geometries have solitonlike solutions with slowly varying amplitudes, similar to those observed in [90]. We consider a two-dimensional (2D) scenario in which the primary blood vessel emitting tip cells and the hypoxic region is situated along separated parallel vertical lines, such that we may average the PDEs along the vertical direction to obtain a 1D approximation. Numerical simulations of the resulting LO-PDEs show that solitons are attractors for intermediate times until they arrive at the neighborhood of the hypoxic region. Solitonlike solutions were previously found in continuum PDE descriptions of hybrid stochastic angiogenesis models [90,91,94].

The paper is organized as follows. In Sec. II, we describe the leading order dynamics of different coarse-grained discrete angiogenesis models and its relation to a hybrid stochastic model. In Sec. III, we describe the approximation of the numerical solutions of the LO-PDEs by a solitonlike wave. We derive the collective coordinate equations (CCEs) that govern the shape and velocity of the soliton. For a given simple linear profile of the tumor angiogenic factor (TAF), we find in Sec. IV that the soliton position is well approximated by the CCEs but its shape is not. This shortcoming stems from ignoring the transversal modulation of the TAF profile in a 2D setting. Section V shows that the CCEs accurately predict the shape and motion of the soliton for a quasisteady Gaussian TAF profile. This is true after a short transient formation stage and until the soliton arrives at the tumor. Increasing the distance between the primary vessel and tumor enlarges the time interval over which the CCEs provide accurate approximations to the soliton dynamics, as shown in Sec. VI. In Sec. VII, we discuss the effect of tip-to-tip anastomosis on soliton evolution. Lastly, Sec. VIII is devoted to concluding remarks.

II. CONTINUUM MODEL

A. Leading order equations

We consider the leading order angiogenesis model derived in [95], under the assumptions of chemotaxis-dominated tip cell movement and relatively low branching rates. This 2D continuum model is described by the following dimensionless coupled LO-PDEs

$$\frac{\partial N}{\partial t} = D\nabla^2 N - \chi \nabla \cdot (N \nabla C) + \lambda N \frac{C}{1+C} - \mu\, a_e N E - \mu\, a_n N^2, \tag{1a}$$

$$\frac{\partial E}{\partial t} = \mu\, N, \tag{1b}$$

for $\mathbf{x} = (x, y)$, with $0 < x < L_x$ and $0 < y < L_y$. The primary vessel and the tumor are located at $x = 0$ and $x = L_x$, respectively (see Fig. 1 for a schematic cartoon of this setup). Here $C(\mathbf{x}, t)$, $N(\mathbf{x}, t)$, and $E(\mathbf{x}, t)$ denote the TAF concentration, the density of tip cells, and the density of stalk cells, respectively. The positive parameter D is the diffusion coefficient of tip cells, and corresponds to the influence of random movement, χ is the chemotactic sensitivity of tip cells, λ is the rate at which branching of new sprouts occurs, and μ is a baseline rate of anastomosis that is further modulated by the values of a_e and a_n, which denote the specific rates of tip-to-sprout and tip-to-tip anastomosis, respectively.

Tip and stalk cell densities are driven by a 2D TAF field (see below and Fig. 1). However, all terms depending on C in Eq. (1a) can be reduced to one spatial variable by column

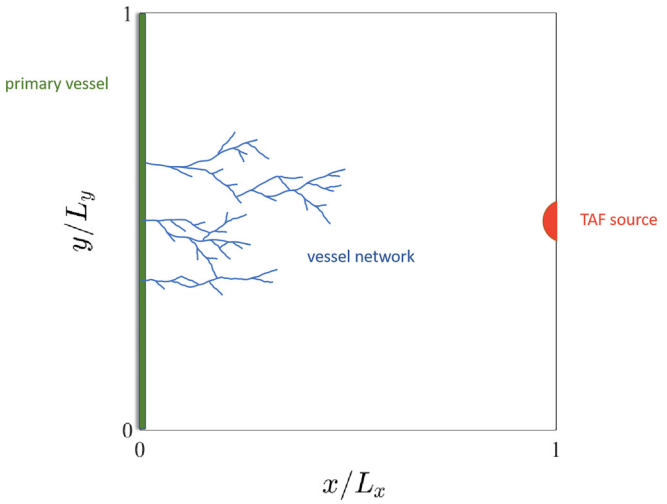

FIG. 1. Sketch of the geometry showing how blood vessels sprout from the primary vessel at $x = 0$ and move to the source of TAF at $x = L_x$.

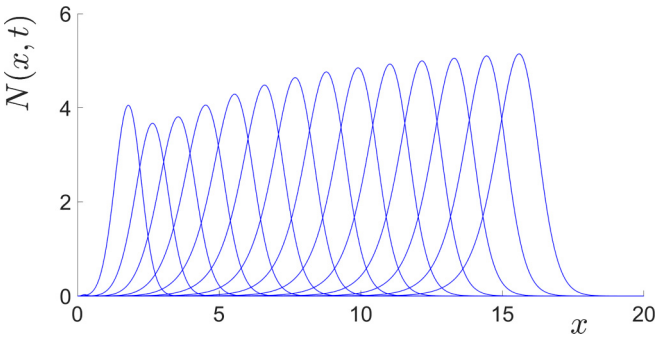

FIG. 2. Snapshots of the tip cell density taken at times $4 + j(\Delta t)$ (with $\Delta t = 2$) between $t = 4$ and $t = 30$, $j = 0, 1, \ldots, 13$. They have been numerically computed by means of Eq. (2), assuming a quasisteady, 1D linear TAF concentration $C(x) = x$ and $L_x = 20$. The scale on the vertical axis is $\times 10^{-5}$.

averaging (namely, averaging in the y direction) in the same fashion as discussed in [95]. The different terms on the right-hand-side of Eq. (1a) describe random diffusion, chemotaxis, tip branching, tip-to-sprout anastomosis, and tip-to-tip anastomosis, while the time evolution of stalk cells is given by a production term depending on tip cell density according to Eq. (1b). The LO-PDE (1b) was derived in [95] and it does not include flux of tip cells and production of stalk cells due to anastomosis [92], which are of higher order. The branching term in Eq. (1a) saturates as $C \to \infty$, which is more realistic than the term linear in C used in Ref. [95]. In this paper, we want to describe the evolution of traveling waves until they arrive near the hypoxic region, but not their interaction with the latter. Thus, we impose no-flux boundary conditions for the tip cell density [95] and do not study the interaction of the waves with the boundary. Such a study would require using more realistic boundary conditions at $x = L_x$. We impose the same nonnegative functions as in [95] to represent the initial conditions for N and E.

The column-averaged PDEs in one spatial variable derived from Eq. (1), together with the boundary and initial conditions, are

$$\frac{\partial N}{\partial t} = D\frac{\partial^2 N}{\partial x^2} - \chi\frac{\partial}{\partial x}\left(N\frac{\partial C}{\partial x}\right) + \lambda N\frac{C}{1+C} - \mu\, a_e NE - \mu\, a_n N^2, \tag{2a}$$

$$\frac{\partial E}{\partial t} = \mu\, N, \tag{2b}$$

$$D\frac{\partial N}{\partial x} - \chi N\frac{\partial C}{\partial x} = 0 \quad \text{at } x = 0,\ L_x, \tag{2c}$$

$$N(x,0) = G(x), \quad E(x,0) = H(x). \tag{2d}$$

Strictly speaking, column averaging gives a solution equivalent to that of the 2D equations only when the TAF field does not vary in the direction transversal to the traveling front. However, the authors found in [95] that there were some situations in which the TAF field did vary in the y direction but the numerical solution of the column averaged model accurately represented that of the full 2D model. Numerical simulations of Eq. (2) are performed after discretizing the spatial derivatives with centered finite differences on a uniform mesh and by using the MATLAB solver `ode15s` for time integration. Figure 2 shows the tip cell density evolution over time for $L_x = 20$ and the following set of parameter values consistent with chemotaxis dominated transport, small diffusion and relatively low branching rate [91]: $D = 0.04$, $\chi = 0.24$, $\lambda = 0.73$, $\mu = 236$, $a_e = 0.14$, and $a_n = 0$. These values will be used throughout the paper, unless otherwise stated. In this case, a source of TAF is assumed to be located at $x = L_x$, considering a quasisteady, one-dimensional (1D) linear concentration $C(x) = x$. A wave is generated at $x = 0$ and travels forward in the direction of the TAF gradient. Indeed, this is a 1D continuum, macroscopic description of the underlying stochastic process detailed in [95] and references therein. Tip cells sprout from a primary vessel at $x = 0$ and migrate toward the right, attracted by the TAF source. They randomly branch and anastomose, thus generating a vascular network.

B. Hybrid stochastic tip cell model equations

From the hybrid stochastic tip cell model of [65,85], we can track the density of active tip cells, $p(\mathbf{x}, \mathbf{v}, t)$, and the TAF concentration, $C(\mathbf{x}, t)$, by ensemble averages over realizations of the stochastic process [89]. Active tip cells are those moving or branching out at a given time. When an active tip cell meets the trajectory of another tip cell, it anastomoses, stops there, and ceases to exist. Then, we may derive the following nondimensional PDE model [89,96]

$$\begin{aligned}\frac{\partial}{\partial t}p(\mathbf{x},\mathbf{v},t) &= \alpha(C(\mathbf{x},t))\delta_{\sigma_v}(\mathbf{v}-\mathbf{v}_0)p(\mathbf{x},\mathbf{v},t)\\ &\quad - \Gamma p(\mathbf{x},\mathbf{v},t)\int_0^t ds\int_{\mathbb{R}^2} d\mathbf{v}' p(\mathbf{x},\mathbf{v}',s)\\ &\quad - \mathbf{v}\cdot\nabla_{\mathbf{x}}p(\mathbf{x},\mathbf{v},t) + \beta\,\mathrm{div}_{\mathbf{v}}(\mathbf{v}p(\mathbf{x},\mathbf{v},t))\\ &\quad - \mathrm{div}_{\mathbf{v}}[\mathbf{F}(C(\mathbf{x},t))p(\mathbf{x},\mathbf{v},t)]\\ &\quad + \frac{\beta}{2}\Delta_{\mathbf{v}}p(\mathbf{x},\mathbf{v},t),\end{aligned} \tag{3a}$$

$$\frac{\partial}{\partial t}C(\mathbf{x},t) = \kappa\,\Delta_{\mathbf{x}}C(\mathbf{x},t) - \chi C(\mathbf{x},t)j(\mathbf{x},t), \tag{3b}$$

$$p(\mathbf{x},\mathbf{v},0) = p_0(\mathbf{x},\mathbf{v}), \quad C(\mathbf{x},0) = C_0(\mathbf{x}), \tag{3c}$$

where

$$\alpha(C(\mathbf{x},t)) = \frac{A\,C(\mathbf{x},t)}{1+C(\mathbf{x},t)},$$

$$\mathbf{F}(C(\mathbf{x},t)) = \frac{\delta_1\nabla_{\mathbf{x}}C(\mathbf{x},t)}{(1+\Gamma_1 C(\mathbf{x},t))^{q_1}},$$

$$\delta_{\sigma_v}(\mathbf{v}-\mathbf{v}_0) = \frac{1}{\pi\sigma_v^2}\,e^{-\frac{|\mathbf{v}-\mathbf{v}_0|^2}{\sigma_v^2}}, \tag{3d}$$

$$j(\mathbf{x},t) = \int_{\mathbb{R}^2}\frac{|\mathbf{v}|}{1+e^{(|\mathbf{v}-\mathbf{v}_0|^2-\eta)/\epsilon}}p(\mathbf{x},\mathbf{v},t)\,d\mathbf{v},$$

$$\tilde{p}(\mathbf{x},t) = \int_{\mathbb{R}^2} p(\mathbf{x},\mathbf{v},t)\,d\mathbf{v}, \tag{3e}$$

for $\mathbf{x}\in\Omega\subset\mathbb{R}^2$, $\mathbf{v}\in\mathbb{R}^2$, $t\in[0,\infty)$. The dimensionless parameters $\beta,\Gamma,\kappa,\chi,A,\Gamma_1,\delta_1,\eta,\epsilon,q_1$ and σ_v are positive. The integral sink term $-\Gamma p\int_0^t\tilde{p}(\mathbf{x},s)ds$ [in which $\tilde{p}$ defined in Eq. (3e) is the marginal tip density] captures the phenomenon that a vessel tip ceases to be active when it encounters another vessel and anastomoses. The anastomosis coefficient Γ is calculated by comparison to numerical simulations of the stochastic process, in such a way that the ensemble average of the total number of active tips equals $\int\tilde{p}(\mathbf{x},t)d\mathbf{x}$. The Gaussian function in Eq. (3d) selects the direction of motion and velocity of new active tips generated by branching. In Eq. (3b), TAF diffuses and is consumed by the flux of advancing tip cells, $j(\mathbf{x},t)$. For the slab geometry of Fig. 1, appropriate nonlocal boundary conditions for $p(\mathbf{x},\mathbf{v},t)$ and boundary conditions for $C(\mathbf{x},t)$ are indicated in [96]. There an appropriate explicit finite-difference numerical scheme is described, and its stability and convergence are proved. Numerical simulations of the PDEs illustrating the formation of a soliton solution and comparison with the solution of the stochastic model can also be found in [96]. Global existence, uniqueness and well-posedness results for Eq. (3) can be found in [97,98].

In the overdamped limit (small inertia), it is possible to obtain a simpler equation for the density of active tip cells $\tilde{p}(\mathbf{x},t)$ [90,91],

$$\frac{\partial\tilde{p}}{\partial t} + \nabla\cdot(\mathbf{F}\,\tilde{p}) - \frac{1}{2\beta}\nabla^2\tilde{p} = \tilde{\mu}\,\tilde{p} - \Gamma\,\tilde{p}\int_0^t\tilde{p}(\mathbf{x},s)\,ds, \tag{4a}$$

$$\frac{\partial C}{\partial t} = \kappa\nabla^2 C - \tau C\,\tilde{p}, \tag{4b}$$

$$\mathbf{F} = (F_x,F_y) = \frac{\delta_1}{\beta}\frac{\nabla C}{1+\Gamma_1 C}, \tag{4c}$$

where $\tau=|\mathbf{v}_0|\chi$, we have set $q_1=1$, and $\tilde{\mu}$ is a function of C related to branching (see [91]). These equations need to be supplemented with initial and boundary conditions appropriate for the configuration that we study. Similarly to previous works [65,85,89–91], we consider a strip geometry with a vertical primary vessel at $x=0$ and a TAF source located at $x=L_x$, as sketched in Fig. 1. Note that $\tilde{p}(\mathbf{x},t)$ and $\int_0^t\tilde{p}(\mathbf{x},s)ds$ in Eq. (4a) correspond to $N(\mathbf{x},t)$ and $E(\mathbf{x},t)$ in Eq. (1), provided tip-to-tip anastomosis is ignored ($a_n=0$) and there are no stalk cells initially [$H(x)=0$ in Eq. (2d)].

After a transient stage, the density of active tips $\tilde{p}(\mathbf{x},t)$ evolves to a solitonlike wave with slowly varying velocity and size, which we can describe by a combination of asymptotics and numerical simulations [90,91]. This stage ends when the soliton approaches the tumor at $x=L_x$.

III. SOLITON DESCRIPTION

In order to characterize the evolution of the tip cell density N, we seek a wavelike approximation for the LO-PDEs in Eqs. (1) and (2). Following the discussion in [91], the soliton has the form

$$N_s(x,t) = \frac{(2Ka_e+\tilde{\mu}^2)c}{2a_e(c-F_x)}\mathrm{sech}^2\left(\frac{\sqrt{2Ka_e+\tilde{\mu}^2}}{2(c-F_x)}\xi\right), \tag{5}$$

where

$$F_x = \chi\,\frac{\partial C}{\partial x}, \quad \tilde{\mu} = \lambda\,\frac{C}{1+C}, \quad \xi = x - X\,. \tag{6}$$

Note that, when C varies slowly in time and space, F_x and $\tilde{\mu}$ in Eq. (6) are suitable average values (see below). On the other hand, $K(t)$, $c(t)$ and $X(t)$ are time-dependent collective coordinates describing the shape and velocity of the soliton. They will be computed by integrating a system of three coupled ordinary differential equations. Thus, Eq. (5) yields a slowly varying solitonlike approximation of the tip cell density, which is valid after a formation stage and far away from the boundary $x=L_x$ where the TAF source is located (see [91]).

Now, following the illustration given in [91], we shall deduce the system of CCEs for the LO-PDEs under the assumptions of small diffusion and a TAF concentration that varies slowly in space and time. First, we observe that N_s is a function of ξ, and the space and time variables through C, namely

$$N_s = N_s\left(\xi;K,c,\tilde{\mu}(C),F_x\left(\frac{\partial C}{\partial x}\right)\right). \tag{7}$$

We assume that the TAF variations over time and space produce terms that are small compared to $\partial N_s/\partial\xi$. In addition, we suppose that $\tilde{\mu}(C)$ is approximately constant (since C is slowly varying) and ignore $\partial^2 N_s/\partial i\partial j$ for $i,j=K,F_x$. Then, plugging Eq. (5) into Eq. (1a), noting that Eq. (1a) has a soliton solution for zero diffusion and constant ∇C, and taking Eq. (7) into account, we obtain

$$\frac{\partial N_s}{\partial K}\dot{K} + \frac{\partial N_s}{\partial c}\dot{c} = \mathcal{A}, \tag{8}$$

where

$$\mathcal{A} = D\frac{\partial^2 N_s}{\partial\xi^2} - N_s\nabla\cdot\mathbf{F} - \frac{\partial N_s}{\partial F_x}[\mathbf{F}\cdot\nabla F_x - D\nabla^2 F_x]$$
$$+ 2D\frac{\partial^2 N_s}{\partial\xi\,\partial F_x}\frac{\partial F_x}{\partial x} - \mu\,a_n N_s^2, \tag{9}$$

with $\mathbf{F}=\chi\nabla C$. Indeed, all terms in Eq. (9) depending on $\mathbf{F}$ or F_x (hence on C) are reduced to the spatial variable x by averaging in the y direction, as mentioned before (see [95]).

Next, we multiply Eq. (8) by $\partial N_s/\partial K$ and integrate over x. We consider a fully formed soliton, far from the primary vessel and the TAF source. As it exponentially decays for $|\xi| \gg 1$, the soliton is regarded to be localized on some finite interval $(-\mathcal{L}/2, \mathcal{L}/2)$, where the TAF varies slowly. Therefore, we can make the approximation [91]

$$\int_{\mathcal{I}} \phi(N_s(\xi;x,t),x)dx \approx \frac{1}{\mathcal{L}} \int_{\mathcal{I}} \left(\int_{-\mathcal{L}/2}^{\mathcal{L}/2} \phi(N_s(\xi;x,t),x)d\xi \right) dx, \tag{10}$$

where the interval $\mathcal{I}$ has extension equal to $\mathcal{L}$ and should contain most of the soliton (here ϕ is a generic function of N_s and x). Thus, the CCEs only hold after an initial soliton formation stage and far from the TAF source region that must be excluded from $\mathcal{I}$. Similarly, we multiply Eq. (8) by $\partial N_s/\partial c$ and integrate over x. From the two resulting formulas, we then find $\dot{K}$ and $\dot{c}$. Since the factor $1/\mathcal{L}$ cancels out and the soliton tails decay to zero, we can set $\mathcal{L} \to \infty$ and obtain the following CCEs [91]:

$$\dot{K} = \frac{\int_{-\infty}^{\infty} \frac{\partial N_s}{\partial K} \mathcal{A}\, d\xi \int_{-\infty}^{\infty} \left(\frac{\partial N_s}{\partial c}\right)^2 d\xi \; - \int_{-\infty}^{\infty} \frac{\partial N_s}{\partial c} \mathcal{A}\, d\xi \int_{-\infty}^{\infty} \frac{\partial N_s}{\partial K} \frac{\partial N_s}{\partial c} d\xi}{\int_{-\infty}^{\infty} \left(\frac{\partial N_s}{\partial K}\right)^2 d\xi \int_{-\infty}^{\infty} \left(\frac{\partial N_s}{\partial c}\right)^2 d\xi \; - \left(\int_{-\infty}^{\infty} \frac{\partial N_s}{\partial c} \frac{\partial N_s}{\partial K} d\xi\right)^2}, \tag{11a}$$

$$\dot{c} = \frac{\int_{-\infty}^{\infty} \frac{\partial N_s}{\partial c} \mathcal{A}\, d\xi \int_{-\infty}^{\infty} \left(\frac{\partial N_s}{\partial K}\right)^2 d\xi \; - \int_{-\infty}^{\infty} \frac{\partial N_s}{\partial K} \mathcal{A}\, d\xi \int_{-\infty}^{\infty} \frac{\partial N_s}{\partial K} \frac{\partial N_s}{\partial c} d\xi}{\int_{-\infty}^{\infty} \left(\frac{\partial N_s}{\partial K}\right)^2 d\xi \int_{-\infty}^{\infty} \left(\frac{\partial N_s}{\partial c}\right)^2 d\xi \; - \left(\int_{-\infty}^{\infty} \frac{\partial N_s}{\partial c} \frac{\partial N_s}{\partial K} d\xi\right)^2}, \tag{11b}$$

together with

$$\dot{X} = c\,. \tag{11c}$$

In these equations, all terms depending on C that vary slowly with x are averaged over the interval $\mathcal{I}$, which will be specified in the sections devoted to the numerical results. On the other hand, the penultimate term in Eq. (9) is odd in ξ and does not contribute to the integrals in Eqs. (11a) and (11b). Most of these integrals have been calculated in Appendix D in [91]. The only two new integrals correspond to the last term in Eq. (9), which models tip-to-tip anastomosis, and they are

$$\int_{-\infty}^{\infty} \frac{\partial N_s}{\partial K} N_s^2 \, d\xi \;=\; \frac{4c^3(2Ka_e + \tilde{\mu}^2)^{\frac{3}{2}}}{9a_e^2(c-F_x)^2}, \tag{12}$$

$$\int_{-\infty}^{\infty} \frac{\partial N_s}{\partial c} N_s^2 d\xi = \frac{4c^2(c-3F_x)(2Ka_e + \tilde{\mu}^2)^{\frac{5}{2}}}{45a_e^3(c-F_x)^3}. \tag{13}$$

These integrals will be relevant to the analysis reported in Sec. VII.

IV. ONE-DIMENSIONAL LINEAR TAF

We first assume, as in Figure 2, that a quasisteady, 1D linear TAF concentration

$$C(x) = x, \tag{14}$$

for $0 < x < 20$, drives the dynamics. Then, we seek a soliton approximation for the tip cell density N as illustrated in Sec. III. The model parameters are set to the values indicated in Sec. II. Moreover, the initial conditions for the CCEs in Eq. (11) are given at $t_0 = 10$ (estimated as the soliton formation stage) as follows: $X(t_0)$ is the location of the maximum of N at t_0, $c(t_0) = X(t_0)/t_0$, and $K(t_0)$ is determined so that the soliton peak coincides with the maximum tip cell density at t_0. After solving the CCEs, the soliton in Eq. (5) is reconstructed and compared to the dynamics of N given by the numerical solutions of Eq. (2).

Figure 3 shows the position and value of the peak (i.e., the maximum) tip cell density as computed by numerical simulations of Eq. (2) and the soliton in Eq. (5). We can observe that, while the peak location is well predicted in the time interval $10 \leqslant t \leqslant 22$, the approximation of the maximum value of N fails. This is due to the simple form of the TAF concentration in Eq. (14). If $C = x$, then the terms in Eq. (9) that depend on advection (i.e., differentials of **F**) vanish and do not contribute to the CCEs. However, these

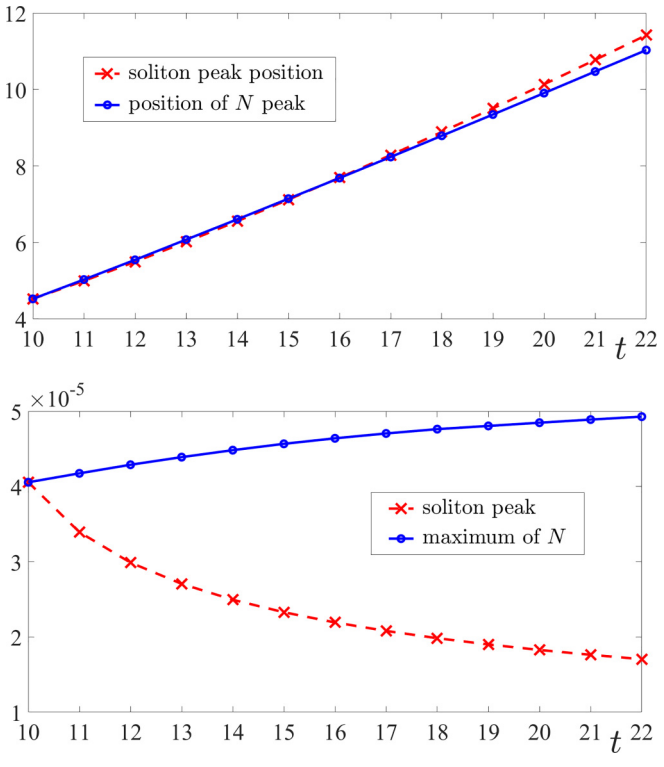

FIG. 3. Time evolution of position (top) and value (bottom) of the maximum tip cell density N as computed by solving Eq. (2) (solid, blue line) and the soliton in Eq. (5) (dashed, red line), for the TAF concentration in Eq. (14) and $L_x = 20$.

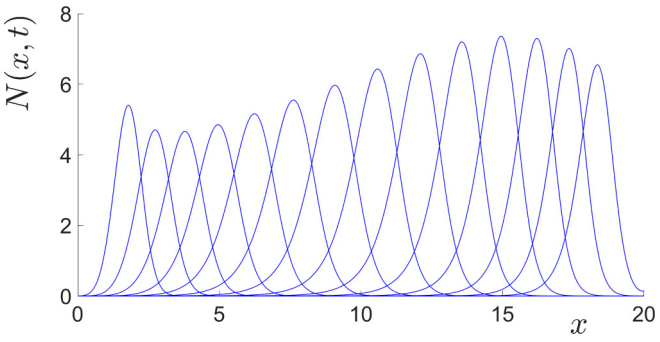

FIG. 4. Counterpart of Fig. 2, for the (column-averaged) TAF concentration in Eq. (15).

terms are crucial for the correct evaluation of the maximum tip density N, which explains the discrepancy shown in Fig. 3.

V. TWO-DIMENSIONAL GAUSSIAN TAF

In order to improve the soliton approximation, we now assume that the quasisteady TAF concentration is a 2D Gaussian [91]:

$$C(x,y) = a\, e^{-(x-21)^2/\sigma_x^2-(y-0.5)^2/\sigma_y^2}, \tag{15}$$

for $0 < x < 20$ and $0 < y < 1$, with $a = 30$, $\sigma_x = 15$, and $\sigma_y = 4$. These values are chosen in such a way that the generated soliton wave has a similar velocity and height as the wave generated for the linear profile of Eq. (14).

In Eqs. (9) and (11)–(13) there are terms depending on the 2D TAF concentration. First, we calculate them as functions of x and y on the 2D domain. Second, we column average them to eliminate their dependence on y. Next, we average over $x \in \mathcal{I} = (0, 2]$ all terms in the CCEs that depend on the TAF and we set the initial conditions for the CCEs at $t_0 = 10$. As before, the model parameter values are those indicated in Sec. II. The counterparts of Figs. 2 and 3 are given by Figs. 4 and 5, respectively. Now, both location and value of the peak tip cell density are well predicted by the soliton in Eq. (5) over the time interval $10 \leqslant t \leqslant 18$. Indeed, the TAF concentration in Eq. (15) contributes to all relevant terms in the system of CCEs; cf. Eq. (9). It is worth remarking that the soliton approximation is robust with respect to changing the values of a, σ_x and σ_y in Eq. (15). Finally, we observe that the soliton description is limited to a finite time window: its validity is affected by the no-flux boundary condition for the tip cell density imposed in the model at $x = L_x = 20$.

VI. TWO-DIMENSIONAL TAF ON A LARGER SPATIAL DOMAIN

In this section, we study how the no-flux boundary condition imposed on the tip cell density at $x = L_x$ affects the soliton approximation. Hence, we consider a quasisteady, 2D Gaussian TAF concentration on a larger spatial domain, namely

$$C(x,y) = a\, e^{-(x-41)^2/\sigma_x^2-(y-0.5)^2/\sigma_y^2}, \tag{16}$$

for $0 < x < 40$ and $0 < y < 1$, with $a = 50$, $\sigma_x = 23$, and $\sigma_y = 4$. For the sake of comparison with Sec. V, the parameter

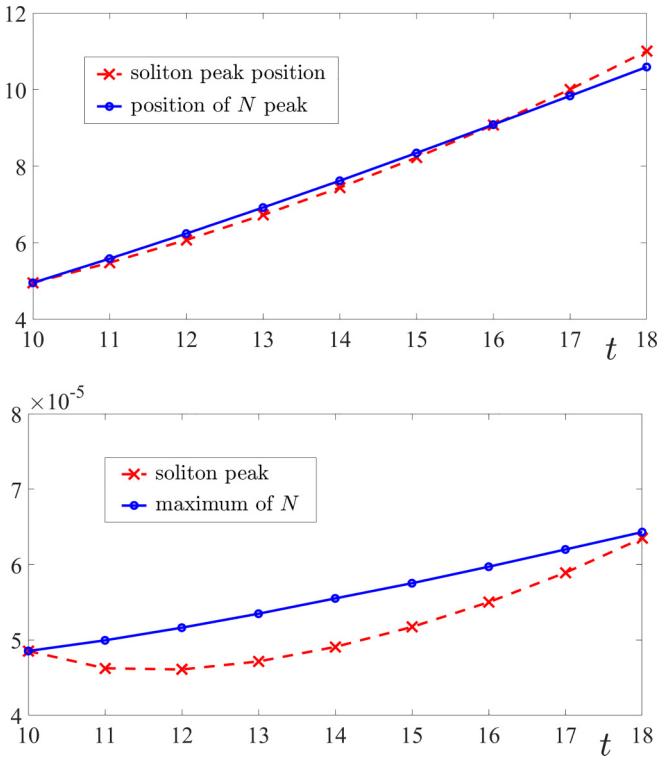

FIG. 5. Counterpart of Fig. 3, for the (column-averaged) TAF concentration in Eq. (15).

values in Eq. (16) have been selected so as to generate [via numerical simulations of Eq. (2)] a tip cell density that reaches its largest maximum at around 75% of the spatial domain in approximately twice the time as in Sec. V; compare Figs. 4 and 6.

Now, the x averages shall be computed in the spatial interval $\mathcal{I} = (0, 4]$, even though restricting the averaging to a small subinterval (e.g., $\mathcal{I} = [3.2, 3.3]$) may result in a slightly better outcome. The model parameters are again set to the values indicated in Sec. II. After an initial stage of $t_0 = 26$ (when the tip cell density reaches its peak at around 25% of the spatial domain, as in the case of Sec. V), the soliton in Eq. (5) is able to predict both location and value of the maximum of N to reasonable accuracy on the time interval $26 \leqslant t \leqslant 42$.

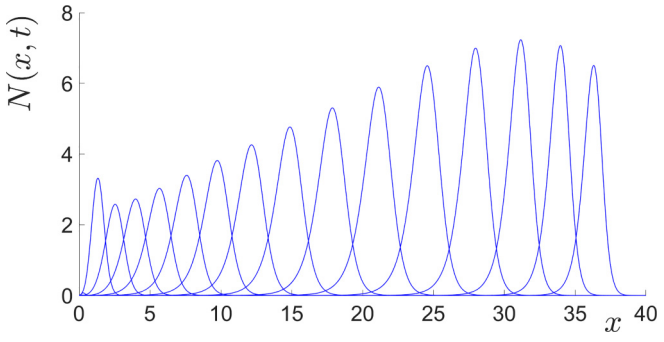

FIG. 6. Snapshots (at distance $\Delta t = 4$) of the time evolution between $t = 4$ and $t = 60$ of the tip cell density as numerically computed from Eq. (2), for the (column-averaged) TAF concentration in Eq. (16) and $L_x = 40$. The scale on the vertical axis is $\times 10^{-5}$.

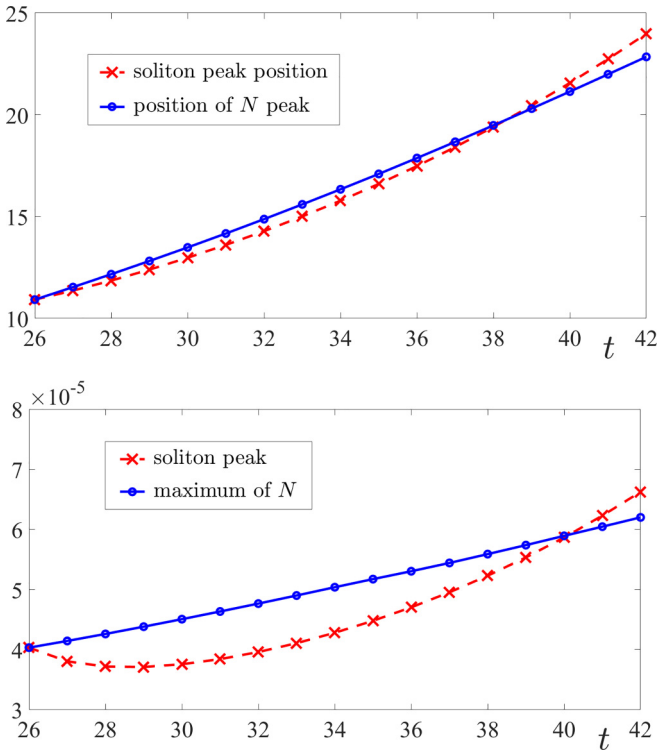

FIG. 7. Counterpart of Fig. 3, for the (column-averaged) TAF concentration in Eq. (16) and $L_x = 40$.

Indeed, the soliton takes longer to reach a point where the effect of the no-flux boundary condition (imposed at $x = 40$ on the tip cell density) starts playing a role. Thus, the soliton approximation holds over a much wider time window, as illustrated in Fig. 7.

VII. EFFECT OF TIP-TO-TIP ANASTOMOSIS

Let us now model tip-to-tip anastomosis by considering $a_n \neq 0$ in Eq. (2). Figure 8 shows the tip cell density evolution over time for the same parameter values as indicated in Sec. II, with ($a_n = 1$) and without ($a_n = 0$) tip-to-tip anastomosis, for the TAF concentration in Eq. (15). Indeed, only a small difference can be appreciated in the overall advance of the wavelike profiles between the two cases. Calibrating the value of the parameter $a_n > 0$ allows modulation of the intensity of this mechanism of vessel fusion.

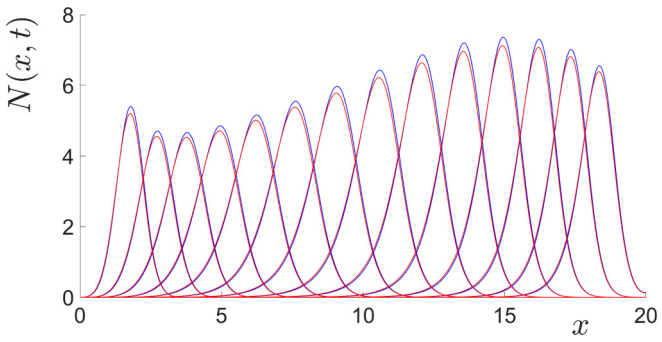

FIG. 8. Counterpart of Fig. 2, for the TAF concentration in Eq. (15), considering $a_n = 0$ (blue lines) and $a_n = 1$ (red lines).

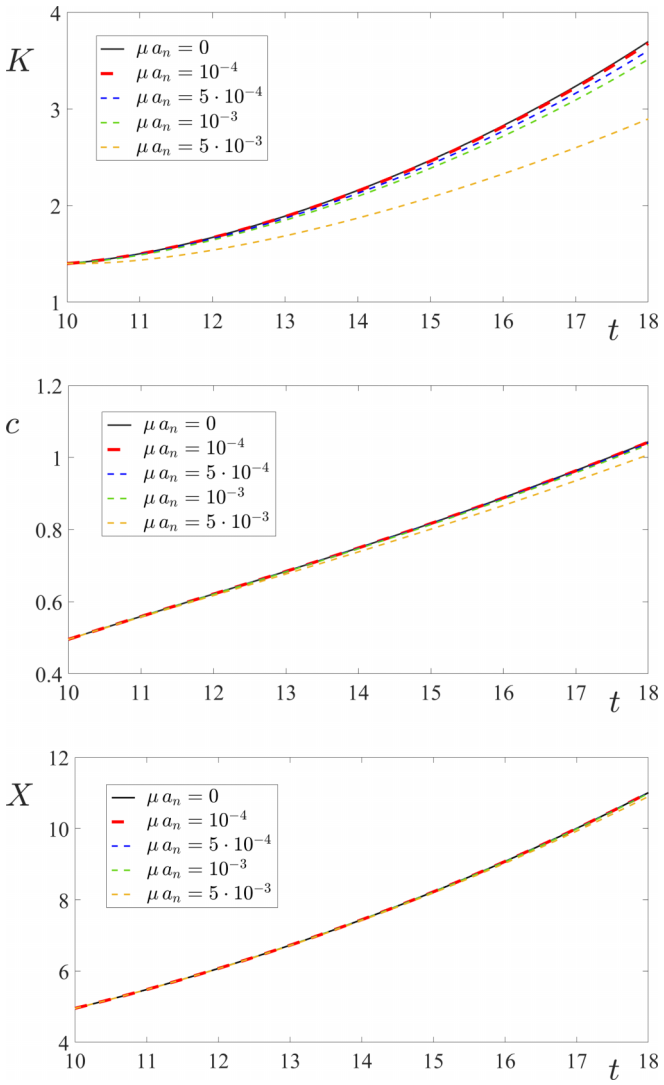

FIG. 9. Temporal evolution of the three collective coordinates, $K(t)$, $c(t)$ and $X(t)$, for the TAF concentration in Eq. (15) and different values of $\mu\, a_n$.

The effect on the soliton approximation can be quantified by taking into account the term $-\mu\, a_n N_s^2$ in Eq. (9), which modifies the CCEs according to the integrals in Eqs. (12) and (13). Considering x averages of the TAF-dependent terms on the spatial interval $\mathcal{I} = (0, 2]$ and initial conditions at $t_0 = 10$, the system of CCEs is integrated in the interval $10 \leqslant t \leqslant 18$ for different values of $\mu\, a_n$ (here, we fix $\mu = 236$ and vary a_n). Figure 9 illustrates the resulting temporal behavior of the three collective coordinates, $K(t)$, $c(t)$ and $X(t)$, in comparison with their evolution for no tip-to-tip anastomosis ($a_n = 0$). We can note that, in the simulated cases, the influence on the overall propagation velocity of the soliton is fairly small. As a consequence, the location of its peak remains unaffected. Undoubtedly, the shape coordinate K is the most sensitive to the presence of the additional term. Indeed, $\mu\, a_n < 5 \times 10^{-3}$ should be considered in order to preserve a soliton description of the tip cell density to within an accuracy similar to the case without tip-to-tip anastomosis (see Sec. V).

VIII. CONCLUDING REMARKS

We have found that the leading order dynamics of ST-PDE and P-PDE systems evolves to a quasi-1D soliton wave after a transient formation stage. The velocity and shape of the soliton are well approximated by CCEs until it approaches the tumor at $x = L_x$. The system of CCEs gives an accurate representation of the soliton shape and motion for a quasisteady Gaussian TAF concentration, whereas the shape is not correctly described if the TAF profile is purely linear. However, we should recall that the 1D LO-PDEs is the result of averaging the corresponding 2D PDEs over the transversal coordinate. When we consider a 2D TAF profile and average it over the transversal coordinate, the soliton wave describes well the velocity and shape of the evolving system of blood vessels.

The LO-PDEs are analogous to the overdamped limit of the continuum equation for the density of active tip cells corresponding to the hybrid stochastic angiogenesis model of [85,89] (which does not include tip-to-tip anastomosis). Thus, the soliton seems to be an attractor for a class of continuum equations resulting from coarse graining different discrete and stochastic angiogenesis models. Provided external fields informing chemotaxis, haptotaxis [65], etc, evolve slowly over longer spatial scales, we can consider their effects by appropriately modifying the CCEs of the soliton [99]. To extend the analysis of the LO-PDEs, we should model a tumor that emits TAF and study its interaction with the arriving soliton wave. This is outside the scope of the present paper.

ACKNOWLEDGMENTS

We acknowledge fruitful discussions with H.M. Byrne. This work has been supported by the FEDER/ Ministerio de Ciencia, Innovación y Universidades – Agencia Estatal de Investigación Grant No. PID2020–112796RB–C22, by the Madrid Government (Comunidad de Madrid, Spain) under the Multiannual Agreement with UC3M in the line of Excellence of University Professors (EPUC3M23), and in the context of the V PRICIT (Regional Programme of Research and Technological Innovation). W.D.M. acknowledges support from the Keasbey Memorial Foundation, the University of Oxford (postgraduate scholarship), and the Advanced Grant Nonlocal-CPD (Nonlocal PDEs for Complex Particle Dynamics: Phase Transitions, Patterns and Synchronization) of the European Research Council Executive Agency (ERC) under the European Union's Horizon 2020 research and innovation programme (Grant Agreement No. 883363). P.K.M. and W.D.M. would like to thank the Isaac Newton Institute for Mathematical Sciences, Cambridge, for support and hospitality during the programme Mathematics of Movement where work on this paper was undertaken. This work was supported by EPSRC Grant No. EP/R014604/1.

[1] *Morphogenesis and Pattern Formation in Biological Systems: Experiments and Models*, edited by T. Sekimura, S. Noji, N. Ueno, and P. K. Maini (Springer, Tokyo, 2003).

[2] P. Friedl and P. D. Gilmour, Collective cell migration in morphogenesis, regeneration and cancer, Nat. Rev. Mol. Cell Biol. **10**, 445 (2009).

[3] A. Ochoa-Espinosa and M. Affolter, Branching morphogenesis: From cells to organs and back, Cold Spring Harb, Perspect. Biol. **4**, a008243 (2012).

[4] S. Alt, P. Ganguly, and G. Salbreux, Vertex models: From cell mechanics to tissue morphogenesis, Phil. Trans. R. Soc. B **372**, 20150520 (2017).

[5] E. Hannezo and B. D. Simons, Multiscale dynamics of branching morphogenesis, Curr. Opin. Cell Biol. **60**, 99 (2019).

[6] J. Li, T. Kim, and D. B. Szymanski, Multi-scale regulation of cell branching: Modeling morphogenesis, Dev. Biol. **451**, 40 (2019).

[7] A. Volkening and B. Stanstede, Iridophores as a source of robustness in zebrafish stripes and variability in Danio patterns, Nat. Commun. **9**, 3231 (2018).

[8] C. J. Weijer, Collective cell migration in development, J. Cell Sci. **122**, 3215 (2009).

[9] A. Okubo, Dynamical aspects of animal grouping: Swarms, schools, flocks, and herds, Adv. Biophys. **22**, 1 (1986).

[10] T. Vicsek and A. Zafeiris, Collective motion, Phys. Rep. **517**, 71 (2012).

[11] A. J. Bernoff and C. M. Topaz, Nonlocal aggregation models: A primer of swarm equilibria, SIAM Rev. **55**, 709 (2013).

[12] A. J. Bernoff and C. M. Topaz, Biological aggregation driven by social and environmental factors: A nonlocal model and its degenerate Cahn-Hilliard approximation, SIAM J. Appl. Dyn. Syst. **15**, 1528 (2016).

[13] A. Cavagna, I. Giardina, T. S. Grigera, The physics of flocking: Correlation as a compass from experiments to theory, Phys. Rep. **728**, 1 (2018).

[14] R. González-Albaladejo, A. Carpio, and L. L. Bonilla, Scale free chaos in the confined Vicsek flocking model, Phys. Rev. E **107**, 014209 (2023).

[15] M. E. Cates, D. Marenduzzo, I. Pagonabarraga, and J. Tailleur, Arrested phase separation in reproducing bacteria creates a generic route to pattern formation, Proc. Natl. Acad. Sci. USA **107**, 11715 (2010).

[16] B. Smeets, R. Alert, J. Pesek, I. Pagonabarraga, H. Ramon, and R. Vincent, Emergent structures and dynamics of cell colonies by contact inhibition of locomotion, Proc. Natl. Acad. Sci. USA **113**, 14621 (2016).

[17] O. A. Igoshin, A. Mogilner, R. D. Welch, D. Kaiser, and G. Oster, Pattern formation and traveling waves in myxobacteria: Theory and modeling, Proc. Natl. Acad. Sci. USA **98**, 14913 (2001).

[18] O. A. Igoshin, R. Welch, D. Kaiser, and G. Oster, Waves and aggregation patterns in myxobacteria, Proc. Natl. Acad. Sci. USA **101**, 4256 (2004).

[19] M. Poujade, E. Grasland-Mongrain, A. Hertzog, J. Jouanneau, P. Chavrier, B. Ladoux, A. Buguin and P. Silberzan, Collective migration of an epithelial monolayer in response to a model wound, Proc. Natl. Acad. Sci. USA **104**, 15988 (2007).

[20] A. Brugués, E. Anon, V. Conte, J. H. Veldhuis, M. Gupta, J. Colombelli, J. J. Muñoz, G. W. Brodland, B. Ladoux, and X. Trepat, Forces driving epithelial wound healing, Nat. Phys. **10**, 683 (2014).

[21] A. Ravasio, I. Cheddadi, T. Chen, T. Pereira, H. T. Ong, C. Bertocchi, A. Brugués, A. Jacinto, A. J. Kabla, Y. Toyama, X. Trepat, N. Gov, L. N. de Almeida, and B. Ladoux, Gap geometry dictates epithelial closure efficiency, Nat. Commun. **6**, 7683 (2015).

[22] P. Friedl, P. B. Noble, P. A. Walton, D. W. Laird, P. J. Chauvin, R. J. Tabah, M. Black, and K. S. Zänker, Migration of coordinated cell clusters in mesenchymal and epithelial cancer explants in vitro, Cancer Res. **55**, 4557 (1995).

[23] P. Friedl and K. Wolf, Tumour-cell invasion and migration: Diversity and escape mechanisms, Nat. Rev. Cancer **3**, 362 (2003).

[24] K. Ganesh, H. Basnet, Y. Kaygusuz, A. M. Laughney, L. He, R. Sharma, K. P. O'Rourke, V. P. Reuter, Y.-H. Huang, M. Turkekul, E. E. Er, I. Masilionis, K. Manova-Todorova, M. R. Weiser, L. B. Saltz, J. Garcia-Aguilar, R. Koche, S. W. Lowe, D. Pe'er, J. Shia, and J. Massagué, L1CAM defines the regenerative origin of metastasis-initiating cells in colorectal cancer, Nature Cancer **1**, 28 (2020).

[25] T. E. Angelini, E. Hannezo, X. Trepat, M. Marquez, J. J. Fredberg, and D. A. Weitz, Glass-like dynamics of collective cell migration, Proc. Natl. Acad. Sci. USA **108**, 4714 (2011).

[26] J.-A. Park, J.-H. Kim, D. Bi, J. A. Mitchel, N. T. Qazvini, K. Tantisira, C. Y. Park, M. McGill, S.-H. Kim, B. Gweon, J. Notbohm, R. Steward Jr, S. Burger, S. H. Randell, A. T. Kho, D. T. Tambe, C. Hardin, S. A. Shore, E. Israel, D. A. Weitz, D. J. Tschumperlin, E. P. Henske, S. T. Weiss, M. L. Manning, J. P. Butler, J. M. Drazen, and J. J. Fredberg, Unjamming and cell shape in the asthmatic airway epithelium, Nat. Mater. **14**, 1040 (2015).

[27] D. Bi, X. Yang, M. C. Marchetti, and M. L. Manning, Motility-driven glass and jamming transitions in biological tissues, Phys. Rev. X **6**, 021011 (2016).

[28] C. Malinverno, S. Corallino, F. Giavazzi, M. Bergert, Q. Li, M. Leoni, A. Disanza, E. Frittoli, A. Oldani, E. Martini, T. Lendenmann, G. Deflorian, G. V. Beznoussenko, D. Poulikakos, K. H. Ong, M. Uroz, X. Trepat, D. Parazzoli, P. Maiuri, W. Yu, A. Ferrari, R. Cerbino, and G. Scita, Endocytic reawakening of motility in jammed epithelia, Nat. Mater. **16**, 587 (2017).

[29] A. Palamidessi, C. Malinverno, E. Frittoli, S. Corallino, E. Barbieri, S. Sigismund, G. V. Beznoussenko, E. Martini, M. Garre, I. Ferrara, C. Tripodo, F. Ascione, E. A. Cavalcanti-Adam, Q. Li, P. P. Di Fiore, D. Parazzoli, F. Giavazzi, R. Cerbino, and G. Scita, Unjamming overcomes kinetic and proliferation arrest in terminally differentiated cells and promotes collective motility of carcinoma, Nat. Mater. **18**, 1252 (2019).

[30] V. Hakim and P. Silberzan, Collective cell migration: A physics perspective, Rep. Prog. Phys. **80**, 076601 (2017).

[31] X. Trepat and E. Sahai, Mesoscale physical principles of collective cell organization, Nat. Phys. **14**, 671 (2018).

[32] P. Carmeliet, Angiogenesis in life, disease and medicine, Nature (London) **438**, 932 (2005).

[33] P. Carmeliet and R. K. Jain, Molecular mechanisms and clinical applications of angiogenesis, Nature (London) **473**, 298 (2011).

[34] R. F. Gariano and T. W. Gardner, Retinal angiogenesis in development and disease, Nature (London) **438**, 960 (2005).

[35] M. Fruttiger, Development of the retinal vasculature, Angiogenesis **10**, 77 (2007).

[36] P. Carmeliet and M. Tessier-Lavigne, Common mechanisms of nerve and blood vessel wiring, Nature (London) **436**, 193 (2005).

[37] M. Potente, H. Gerhardt, and P. Carmeliet, Basic and therapeutic aspects of angiogenesis, Cell **146**, 873 (2011).

[38] A. Szymborska and H. Gerhardt, Hold me, but not too tight - endothelial cell-cell junctions in angiogenesis, Cold Spring Harb. Perspect. Biol. **10**, a029223 (2018).

[39] J. Folkman, Tumor angiogenesis: Therapeutical implications, N. Engl. J. Med. **285**, 1182 (1971).

[40] H. M. Byrne, Dissecting cancer through mathematics: From the cell to the animal model, Nat. Rev. Cancer **10**, 221 (2010).

[41] N. Sawada and Z. Arany, Metabolic regulation of angiogenesis in diabetes and aging, Physiology **32**, 290 (2017).

[42] Y. M. Paulus and A. Sodhi, Anti-angiogenic therapy for retinal disease, Handb. Exp. Pharmacol. **242**, 271 (2017).

[43] R. Vega, M. Carretero, and L. L. Bonilla, Anomalous angiogenesis in retina, Biomedicines **9**, 224 (2021).

[44] T. Omelchenko, J. M. Vasiliev, I. M. Gelfand, H. H. Feder, and E. M. Bonder, Rho-dependent formation of epithelial "leader" cells during wound healing, Proc. Natl. Acad. Sci. USA **100**, 10788 (2003).

[45] N. Sepúlveda, L. Petitjean, O. Cochet, E. Grasland-Mongrain, P. Silberzan, and V. Hakim, Collective cell motion in an epithelial sheet can be quantitatively described by a stochastic interacting particle model, PLoS Comput. Biol. **9**, e1002944 (2013).

[46] L. L. Bonilla, A. Carpio, and C. Trenado, Tracking collective cell motion by topological data analysis, PLoS Comput. Biol. **16**, e1008407 (2020).

[47] L. A. Liotta, G. M. Saidel, and J. Kleinerman, Diffusion model of tumor vascularization and growth, Bull. Math. Biol. **39**, 117 (1977).

[48] D. Balding and D. L. S. McElwain, A mathematical model of tumour-induced capillary growth, J. Theor. Biol. **114**, 53 (1985).

[49] M. A. J. Chaplain and A. M. Stuart, A model mechanism for the chemotactic response of endothelial cells to tumour angiogenesis factor, IMA J. Math. Appl. Med. Biol. **10**, 149 (1993).

[50] H. M. Byrne and M. A. J. Chaplain, Mathematical models for tumour angiogenesis: Numerical simulations and nonlinear wave solutions, Bull. Math. Biol. **57**, 461 (1995).

[51] M. A. J. Chaplain, The mathematical modelling of tumour angiogenesis and invasion, Acta Biotheor **43**, 387 (1995).

[52] A. R. A. Anderson and M. A. J. Chaplain, Continuous and discrete mathematical models of tumor-induced angiogenesis, Bull. Math. Biol. **60**, 857 (1998).

[53] A. L. Bauer, T. L. Jackson, and Y. Jiang, A cell-based model exhibiting branching and anastomosis during tumor-induced angiogenesis, Biophys. J. **92**, 3105 (2007).

[54] A. L. Bauer, T. L. Jackson, and Y. Jiang, Topography of extracellular matrix mediates vascular morphogenesis and migration speeds in angiogenesis, PLoS Comput. Biol. **5**, e1000445 (2009).

[55] K. Bentley, H. Gerhardt, and P. A. Bates, Agent-based simulation of Notch-mediated tip cell selection in angiogenic sprout initialisation, J. Theor. Biol. **250**, 25 (2008).

[56] G. An, Q. Mi, J. Dutta-Moscato, and Y. Vodovotz, Agent-based models in translational systems biology, Wiley Interdiscip. Rev. Syst. Biol. Med. **1**, 159 (2009).

[57] P. Van Liedekerke, M. M. Palm, N. Jagiella, and D. Drasdo, Simulating tissue mechanics with agent-based models: Concepts, perspectives and some novel results, Comp. Part. Mech. **2**, 401 (2015).

[58] J. M. Osborne, A. G. Fletcher, J. M. Pitt-Francis, P. K. Maini, and D. J. Gavaghan, Comparing individual-based approaches to modelling the self-organization of multicellular tissues, PLoS Comput. Biol. **13**, e1005387 (2017).

[59] J. Metzcar, Y. Wang, R. Heiland, and P. Macklin, A review of cell-based computational modeling in cancer biology, JCO Clin. Cancer Informatics **3**, 1 (2019).

[60] E. G. Rens and R. M. H. Merks, Cell shape and durotaxis explained from cell-extracellular Matrix forces and focal adhesion dynamics, iScience **23**, 101488 (2020).

[61] R. Vega, M. Carretero, R. D. M. Travasso, and L. L. Bonilla, Notch signaling and taxis mechanims regulate early stage angiogenesis: A mathematical and computational model, PLoS Comput. Biol. **16**, e1006919 (2020).

[62] D. Stepanova, H. M. Byrne, P. K. Maini, and T. Alarcón, A multiscale model of complex endothelial cell dynamics in early angiogenesis, PLoS Comp. Biol. **17**, e1008055 (2021).

[63] S. Jafari Nivlouei, M. Soltani, J. Carvalho, R. Travasso, M. Reza Salimpour, and E. Shirani, Multiscale modeling of tumor growth and angiogenesis: Evaluation of tumor-targeted therapy, PLoS Comput. Biol. **17**, e1009081 (2021).

[64] N. Bellomo and A. Bellouquid, On the derivation of angiogenesis tissue models: From the micro-scale to the macro-scale, Math. Mech. Solids **20**, 268 (2015).

[65] V. Capasso and D. Morale, Stochastic modelling of tumour-induced angiogenesis, J. Math. Biol. **58**, 219 (2009).

[66] K. A. Rejniak and A. R. A. Anderson, Hybrid models of tumor growth, Wiley Interdiscip. Rev. Syst. Biol. Med. **3**, 115 (2011).

[67] R. D. M. Travasso, E. Corvera Poiré, M. Castro, J. C. Rodríguez-Manzaneque, and A. Hernández-Machado, Tumor angiogenesis and vascular patterning: A mathematical model, PLoS ONE **6**, e0019989 (2011).

[68] M. J. Plank and B. D. Sleeman, Lattice and non-lattice models of tumour angiogenesis, Bull. Math. Biol. **66**, 1785 (2004).

[69] N. V. Mantzaris, S. Webb, H. G. Othmer, Mathematical modeling of tumor-induced angiogenesis, J. Math. Biol. **49**, 111 (2004).

[70] A. A. Qutub, F. Mac Gabhan, E. D. Karagiannis, P. Vempati, and A. S. Popel, Multiscale models of angiogenesis: Integration of molecular mechanisms with cell- and organ-level models, IEEE Eng. Med. Biol. Mag. **28**, 14 (2009).

[71] M. Scianna, C. G. Bell, and L. Preziosi, A review of mathematical models for the formation of vascular networks, J. Theor. Biol. **333**, 174 (2013).

[72] G. Vilanova, I. Colominas, and H. Gomez, Coupling of discrete random walks and continuous modeling for three-dimensional tumor-induced angiogenesis, Comput. Mech. **53**, 449 (2014).

[73] T. A. M. Heck, M. M. Vaeyens, H. Van Oosterwyck, Computational models of sprouting angiogenesis and cell migration: Towards multiscale mechanochemical models of angiogenesis, Math. Model. Nat. Phenom. **10**, 108 (2015).

[74] F. Spill, P. Guerrero, T. Alarcón, P. K. Maini, and H. M. Byrne, Mesoscopic and continuum modelling of angiogenesis, J. Math. Biol. **70**, 485 (2015).

[75] G. Vilanova, I. Colominas, and H. Gomez, Computational modeling of tumor-induced angiogenesis, Arch. Computat. Methods Eng. **24**, 1071 (2017).

[76] H. Perfahl, B. D. Hughes, T. Alarcón, P. K. Maini, M. C. Lloyd, M. Reuss, and H. M. Byrne, 3D hybrid modelling of vascular network formation, J. Theor. Biol. **414**, 254 (2017).

[77] L. L. Bonilla, M. Carretero, and F. Terragni, Stochastic models of blood vessel growth, *Stochastic dynamics out of equilibrium* (PROMS 282, Springer 2019), pp. 413–436.

[78] J. A. Flegg, S. N. Menon, H. M. Byrne, and D. L. S. McElwain, A current perspective on wound healing and tumour-induced angiogenesis, Bull. Math. Biol. **82**, 23 (2020).

[79] G. J. Pettet, H. M. Byrne, D. L. S. McElwain, and J. Norbury, A model of wound-healing angiogenesis in soft tissue, Math. Biosci. **136**, 35 (1996).

[80] A. J. Connor, R. P. Nowak, E. Lorenzon, M. Thomas, F. Herting, S. Hoert, T. Quaiser, E. Shochat, J. Pitt-Francis, J. Cooper, P. K. Maini, and H. M. Byrne, An integrated approach to quantitative modelling in angiogenesis research, J. R. Soc. Interface **12**, 20150546 (2015).

[81] L. Edelstein, The propagation of fungal colonies: A model for tissue growth, J. Theor. Biol. **98**, 679 (1982).

[82] S. Ishihara, P. Marcq, and K. Sugimura, From cells to tissue: A continuum model of epithelial mechanics, Phys. Rev. E **96**, 022418 (2017).

[83] A. Hernandez and M. C. Marchetti, Poisson-bracket formulation of dynamics of fluids of deformable particles, Phys. Rev. E **103**, 032612 (2021).

[84] G. Triguero-Platero, F. Ziebert, and L. L. Bonilla, Coarse-graining the vertex model and its response to shear, Phys. Rev. E **108**, 044118 (2023).

[85] L. L. Bonilla, V. Capasso, M. Alvaro, and M. Carretero, Hybrid modeling of tumor-induced angiogenesis, Phys. Rev. E **90**, 062716 (2014).

[86] M. Alber, N. Chen, P. M. Lushnikov, and S. A. Newman, Continuous macroscopic limit of a discrete stochastic model for interaction of living cells, Phys. Rev. Lett. **99**, 168102 (2007).

[87] R. E. Baker, C. A. Yates, and R. Erban, From microscopic to macroscopic descriptions of cell migration on growing domains, Bull. Math. Biol. **72**, 719 (2010).

[88] D. C. Markham, M. J. Simpson, and R. E. Baker, Simplified method for including spatial correlations in mean-field approximations, Phys. Rev. E **87**, 062702 (2013).

[89] F. Terragni, M. Carretero, V. Capasso, and L. L. Bonilla, Stochastic model of tumour-induced angiogenesis: Ensemble averages and deterministic equations, Phys. Rev. E **93**, 022413 (2016).

[90] L. L. Bonilla, M. Carretero, F. Terragni, and B. Birnir, Soliton driven angiogenesis, Sci. Rep. **6**, 31296 (2016).

[91] L. L. Bonilla, M. Carretero, and F. Terragni, Solitonlike attractor for blood vessel tip density in angiogenesis, Phys. Rev. E **94**, 062415 (2016).

[92] S. Pillay, H. M. Byrne, and P. K. Maini, Modeling angiogenesis: A discrete to continuum description, Phys. Rev. E **95**, 012410 (2017).

[93] W. D. Martinson, H. M. Byrne, and P. K. Maini, Evaluating snail-trail frameworks for leader-follower behavior with agent-based modeling, Phys. Rev. E **102**, 062417 (2020).

[94] L. L. Bonilla, M. Carretero, and F. Terragni, Two dimensional soliton in tumor induced angiogenesis, J. Stat. Mech. (2020) 083402.

[95] W. D. Martinson, H. Ninomiya, H. M. Byrne, and P. K. Maini, Comparative analysis of continuum angiogenesis models, J. Math. Biol. **82**, 21 (2021).

[96] L. L. Bonilla, A. Carpio, M. Carretero, G. Duro, M. Negreanu, and F. Terragni, A convergent numerical scheme for integrodifferential kinetic models of angiogenesis, J. Comput. Phys. **375**, 1270 (2018).

[97] A. Carpio and G. Duro, Well posedness of an integrodifferential kinetic model of Fokker-Planck type for angiogenesis, Nonlinear Anal. Real World Appl. **30**, 184 (2016).

[98] A. Carpio, G. Duro, and M. Negreanu, Constructing solutions for a kinetic model of angiogenesis in annular domains, Appl. Math. Model. **45**, 303 (2017).

[99] L. L. Bonilla, M. Carretero, and F. Terragni, Ensemble averages, soliton dynamics and influence of haptotaxis in a model of tumor-induced angiogenesis, Entropy **19**, 209 (2017).